Nanoscale

PAPER

View Article Online
View Journal | View Issue

Cite this: *Nanoscale*, 2017, **9**, 11605

Nanoscale steady-state temperature gradients within polymer nanocomposites undergoing continuous-wave photothermal heating from gold nanorods†

Somsubhra Maity,[a] Wei-Chen Wu,[b] Joseph B. Tracy,[b] Laura I. Clarke*[a] and Jason R. Bochinski*[a]

Anisotropically-shaped metal nanoparticles act as nanoscale heaters *via* excitation of a localized surface plasmon resonance, utilizing a photothermal effect which converts the optical energy into local heat. Steady-state temperatures within a polymer matrix embedded with gold nanorods undergoing photothermal heating using continuous-wave excitation are measured in the immediate spatial vicinity of the nanoparticle (referred to as the local temperature) from observing the rate of physical rotation of the asymmetric nanoparticles within the locally created polymer melt. Average temperatures across the entire (mostly solid) sample (referred to as the global temperature) are simultaneously observed using a fluorescence method from randomly dispersed molecular emitters. Comparing these two independent measurements in films having varying concentrations of nanorods reveals the interplay between the local and global temperatures, clearly demonstrating the capability of these material samples to sustain large steady-state spatial temperature gradients when experiencing continuous-wave excitation photothermal heating. These results are discussed quantitatively. Illustrative imaging studies of nanofibers under photothermal heating also support the presence of a large temperature gradient. Photothermal heating in this manner has potential utility in creating unique thermal processing conditions for outcomes such as driving chemical reactions, inducing crystallinity changes, or enhancing degradation processes in a manner unachievable by conventional heating methods.

Received 26th June 2017,
Accepted 18th July 2017

DOI: 10.1039/c7nr04613h

rsc.li/nanoscale

1. Introduction

A metal nanoparticle has a large effective cross section[1,2] for the absorption of light resonant with its localized surface plasmon resonance (LSPR). Although dependent on the size, shape, and composition of the particle as well as the surrounding dielectric environment, for noble metal nanoparticles the LSPR wavelength range conveniently occurs within the visible or near infrared spectral region, where excitation sources are readily available. When an LSPR is excited, a coherent oscillation of conduction electrons occurs. Due to intrinsic losses, the coherent electron motion decays rapidly[3] and irreversibly (in $\lesssim$1 ns *via* a sequential process of electron thermalization, electron–phonon relaxation, and finally, phonon–phonon relaxation) and the absorbed energy is converted into heat. For anisotropically-shaped metal nanoparticles, electron oscillation along different spatial directions creates multiple, spectrally distinct LSPRs, such as the longitudinal (*l*-LSPR) and transverse (*t*-LSPR) resonances present in a gold nanorod (GNR).[4,5] The aspect ratio (AR) of the GNR controls the red-shifted spectral location of the *l*-LSPR as compared to the relatively fixed *t*-LSPR.

Thus, a metal nanoparticle acts as both an efficient receiver of electromagnetic waves (light absorber) and as a nanoscale emitter of heat, effectively condensing the incident light into locally-released thermal energy through this photothermal effect. Dependent upon the coupling between a nanoparticle and its surroundings, the thermal energy propagates away from the nanoscale heater through radiative, convective, and conductive processes, resulting in a temperature change in the surrounding media. Though previously perceived as a parasitic effect, new research directions seek to utilize plasmonically-based photothermal heating within a diversity of fields and

[a]*Department of Physics, North Carolina State University, Raleigh, NC 27695-8202, USA. E-mail: laura_clarke@ncsu.edu, jason_bochinski@ncsu.edu*
[b]*Department of Materials Science and Engineering, North Carolina State University, Raleigh, NC 27695, USA*

†Electronic supplementary information (ESI) available: Fig. S1: TEM image of photothermal- and field-assisted GNR alignment. Fig. S2: Average global sample temperature *versus* time for different GNR concentrations. Fig. S3: Temperature measurements are independent of substrate material or thickness. See DOI: 10.1039/c7nr04613h

applications including chemistry,[6] material catalysis,[7,8] polymer processing,[9–14] solar energy harvesting,[15,16] optical switching[17] and actuation,[18,19] as well as for biomedical uses such as cancer therapy[20] and drug delivery.[21]

Such novel heating applications present a challenging experimental task of accurate temperature measurement with nanoscale resolution.[22–24] Myriad non-contact methods to infer local temperatures near photothermally-active objects have been employed, such a polarization anisotropy,[25] emission spectroscopy,[26–29] absorption spectroscopy,[30,31] conductance measurements,[32] detection of electron spin resonance,[33] and monitoring of irreversible morphological alterations[11,34–36] or reorientation dynamics of anisotropic nanoparticles within a viscous medium.[37] In the present work, comparison of the observed temperature values in the immediate spatial region surrounding GNRs to the average temperature values measured over the entire sample volume reveals the existence of a steady-state gradient within the polymer material. Temperature in the vicinity of the nanorods is determined by monitoring the GNR rotational dynamics while fluorescence from dispersed fluorophores across the entire nanocomposite provides information on the overall average sample temperature.

These results indicate that incorporating metal nanoparticles at low concentrations within a material environment enables such efficacious nanoscale heaters to create a steady-state, inhomogeneous spatial temperature distribution, where the temperature near to the particle (referred to as "local") can be substantively larger than the average temperature in the cooler sample volume regions further removed (referred to as "global"). Such a steady-state temperature gradient has been previously reported in nanocomposite samples experiencing ultrafast femtosecond illumination.[37] Here, a similar temperature distribution is shown to occur under continuous-wave excitation, a result which is in contrast to previous general theoretical predictions[38,39] and measurements within aqueous environments.[40,41] Its presence is independent of the film thickness, nanorod concentration, or substrate material. The gradient is most prominently observed with dilute GNR sample loading, which naturally creates larger average nanoparticle-to-nanoparticle spatial separations. Comparing two significantly different nanoparticle concentrations, at higher loading, the nanorods are relatively closely spaced, leading to an overall average sample temperature that is above the melt temperature (T_m) of the material and relatively close to the peak, highest sample temperature (located near the GNRs). However, at less concentrated loadings, while the sample temperature near the GNRs is sufficient to melt a small surrounding volume of polymer and allow nanorod rotational reorientation, the overall average nanocomposite temperature is significantly cooler ($\ll T_m$); hence, the majority of the film remains rigid and solid. Thus, under photothermal heating of embedded metal nanoparticles utilizing a continuous-wave excitation source, the interplay between the local and global sample temperatures can be manipulated by altering particle concentration. These observations have been made under varying excitation conditions and take advantage of the dual LSPRs available in GNRs to simultaneously use the nanoparticles to both heat and probe the sample local temperature.

An independent method to verify the steady-state temperature gradient is provided by monitoring morphological changes of highly thermally sensitive nanofibrous samples during photothermal heating. Measurements reveal selective local melting of material in the nanoparticle's immediate spatial volume whilst the overall cylindrical fiber shape is preserved, which is also consistent with distinctive local and global temperatures.

2. Results and discussion

2.1 Creating large scale alignment of nanorods within a polymer matrix

Considerable previous research exploring photothermal heating of metal nanoparticles has employed aqueous environments.[41–44] Such experimental focus is due to both the chemical compatibility between easily-fabricated, citrate-stabilized metal nanoparticles and water, as well as the important biomedical research applications of cancer and drug release therapies.[45] Fewer published works have explored using nanoparticles encapsulated within transparent (or thin) solid material samples.[9–14,19] Yet these environments have distinct advantages, particularly when anisotropic nanoparticles are employed, due to the useful ability to control and monitor the particle's orientation throughout thermal processes. Moreover, forming nanocomposites by embedding metal nanoparticles within polymer matrices can create novel materials which have diverse technical applications: for example, having enhanced optical[46–51] or antimicrobial[52] properties, smart[53] or self-healing[54] capabilities, increased photovoltaic efficiency,[55,56] or performing actuation in shape memory[57,58] or liquid crystal[59,60] systems.

The two spectrally distinct LSPRs characteristic of nanorods provide a convenient optical signature to determine GNR alignment within thin nanocomposites samples. Fig. 1 displays normalized polarized extinction measurements for a film sample of polymer (polyethylene oxide (PEO)) containing oriented GNRs. The peak at ~520 nm (~840 nm) corresponds to the spectral location of the *t*-LSPR (*l*-LSPR) for an ensemble of gold nanorods having an AR of ~4 : 1 (68 nm : 17 nm). A sample with oriented GNRs requires not only spectral (*i.e.*, wavelength) but also polarization matching for coupling of light to the different LSPRs.

In Fig. 1, the angle value listed in the legend corresponds to the relative angle between the polarization direction of the probe beam and alignment direction of the longitudinal axis of the GNRs, hence 0° (90°) indicates that the linearly-polarized probe beam being oriented parallel (perpendicular). When rotating the relative polarization direction from 0° to 90°, the peak which corresponds to the *l*-LSPR decreases as the amplitude of *t*-LSPR feature increases. For GNRs dispersed in low viscosity fluids or randomly-oriented within solid film samples, no such angular dependence on the extinction peaks is observed because the nanorod orientation is homogeneous and isotropic.

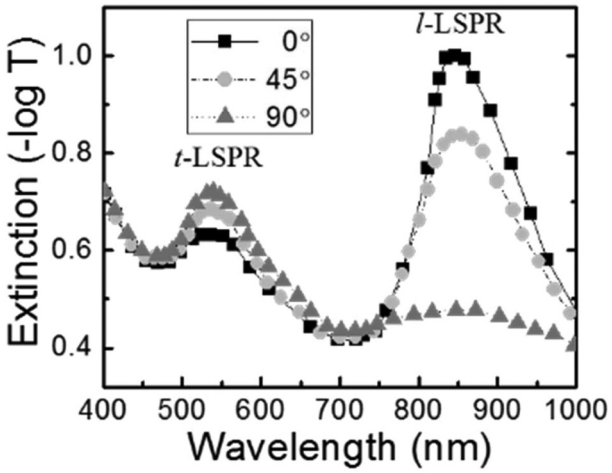

Fig. 1 Normalized polarized extinction *versus* wavelength measurements reveal the spectral locations of the *t*-LSPR (~520 nm) and *l*-LSPR (~840 nm). For nanocomposite PEO : GNR film samples having an ensemble of aligned nanorods (where 0° (90°) corresponds to the linearly-polarized probe beam directed parallel (perpendicular) to the long axis of the GNRs) when rotating the polarization direction from 0° to 90°, the peak corresponding to the *l*-LSPR decreases as the amplitude of *t*-LSPR feature increases.

Achieving orientation of GNRs in nanocomposite films has previously been demonstrated by mechanical means[61,62] or through application of external constant electric fields.[37,63,64] In the present work, variations of the latter approach are implemented to accomplish global ensemble GNR orientation through two related methods, implemented either during initial sample fabrication or in a post-processing manner. For the first approach, an electric field of ~20 kV cm^{-1} is applied across a drop-cast solution consisting of PEO, GNRs, and other additives in a methanol/water solvent mixture during drying (for ~1 hour) *via* solvent evaporation under ambient conditions. The applied field induces a torque on the GNR and thereby reorients the particle toward a preferred alignment with the nanorod longitudinal axis parallel to the electric field. Fig. 2a shows a transmission electron microscopy (TEM) image of randomly-distributed GNRs in a thin, drop-cast PEO film. In contrast, Fig. 2b reveals the effect of applying the electric field during fabrication, producing alignment of the GNRs along the field direction.

For the second approach to create sample-wide nanoparticle alignment, a fully dried, solid polymer film containing randomly-oriented GNRs is illuminated for several minutes by circularly-polarized light resonant with one of the LSPRs in order to photothermally heat all GNRs regardless of orientation, producing melting of the matrix surrounding the nanorods. Simultaneous application of an external electric field subsequently fosters reorientation of the GNRs within the locally molten polymer along the field direction. The electric field is then maintained for one hour after the excitation laser beam is extinguished, and as the polymer melt cools and re-solidifies, the externally-determined, nanorod orientation is

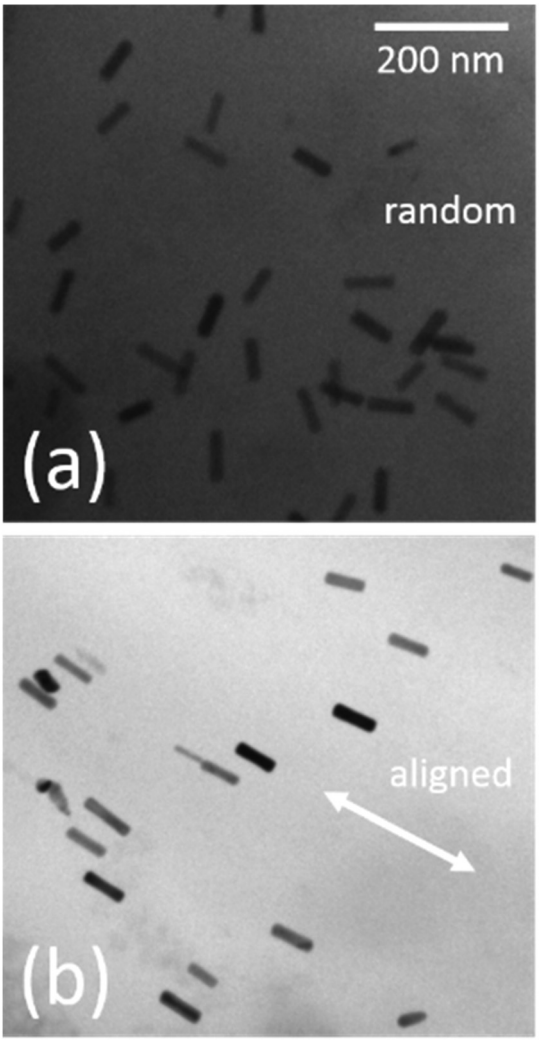

Fig. 2 Electric-field assisted alignment of GNRs. (a) TEM image of an as-fabricated PEO : GNR film with random orientations of nanorods. Scale bar applies to both images. (b) TEM image of PEO : GNR nanocomposite film with an applied electric field of 20 kV cm^{-1} during drying under ambient conditions, creating a global alignment of the nanorods along the field direction, as indicated by the white arrow.

preserved. Comparison of TEM images in ESI Fig. S1a and S1b† show the effectiveness of this second approach, where an excitation source of 4 W cm^{-2} at 514 nm (resonant with the *t*-LSPR of the GNRs) was utilized. Both methods produce the same average high GNR alignment fidelity (0 ± ~9°) in the final nanocomposite samples, as determined by analysis of multiple TEM images.

2.2 Measuring nanoscale temperature through non-contact approaches

Non-contact optical thermometry[65–68] is a general approach to remotely observe thermal processes. Recently, specific methods[37] have been developed to interpret temperature information from polymer nanocomposite samples undergoing photothermal heating of metal nanoparticles using ultrafast

laser excitation. In that previous research, a steady-state temperature gradient was observed where the sample was the hottest at the GNRs and cooler in the direction radially away from the nanoparticles. Similarly, in the results presented here two distinct optical methods are simultaneously employed to detect the steady-state temperature within the polymer nanocomposite while undergoing continuous-wave photothermal heating of the embedded nanorods. Comparison of steady-state temperature information at two locations – in the immediately vicinity of the GNRs and from the average across the entire sample which is heavily weighted toward the cooler regions – reveals a temperature gradient also exists within a polymeric sample under these excitation conditions, though not as extreme in range as under ultra-fast pulsed excitation.

2.2.1 Perylene as molecular temperature reporter. Uniformly dispersed fluorophores within a solid thin film can act as molecular nanoscale temperature sensors and provide a robust, spatially-averaged measurement of sample temperature. As discussed extensively in previous works,[10,12,13,19,37] generally the amplitude and shape of the fluorescence spectrum is reproducibly altered as a function of sample temperature due to an enhanced non-radiative relaxation rate (specifically, a decrease in overall amplitude and broadening in peak width with increasing temperature). Comparing emission amplitude values at two distinct wavelengths provides a ratio measurement which minimizes any spurious effects due to excitation source fluctuations. Analyzing correlations for all possible wavelength ratios from full spectra taken at differing temperatures and assuming (*a priori*) a linear relationship reveals multiple potential ratio pairs. The wavelength ratios with the most linear temperature dependence come from combinations of fluorescence peak wavelengths (peaks) compared against the lower amplitude spectral regions between adjacent peaks (troughs). Since the first, lowest wavelength peak emission (~450 nm in a PEO composite film) is also potentially subject to influence by re-absorption, it is not utilized to avoid sample thickness or fluorophore concentration dependences. Subsequently, a calibration curve of sample temperature *versus* ratio value using the trough between the two lowest wavelength emission peaks and the second fluorescence peak is generated for the particular polymer composite system, as samples are heated using conventional means such as a hot plate.

Under such conventional heating, the sample temperature is largely homogenous and relatively spatially uniform with energy transferring from the sample's surface into the interior; in contrast, under photothermal heating, thermal energy is released locally at the nanoparticles and may create nanoscale temperature inhomogeneity within the sample, where it is hottest at the GNRs and cooler further away, heating the sample from the inside out. While each individual, randomly placed fluorophore has a relaxation rate that is sensitive to its own immediate, unique environment, emission signals from a large ensemble provide a robust and accurate spatially-averaged temperature measurement across the sample. Hence, using the calibration curve, ratio values from conventionally heated samples are compared to those which undergo photothermal heating from metal nanoparticles, which provides a determination of the average sample temperature created under different excitation conditions.

For the well-dispersed perylene molecules, this observation weights the measurement towards the signals from cooler sample regions further removed from GNRs which represents the vast majority of the sample volume (as the nanoparticles typically are introduce at a low loading level of $\leq$~1 weight percent (wt%) within the sample). Depending on the nanoparticle loading, the average particle-to-particle spacing varies from few 100 nm to μm distances.

2.2.2 Direct measurement of GNR rotation. Rotational diffusion of GNRs embedded within a rigid material sample implicitly necessitates that the local volume surrounding the nanoparticle reaches a sufficiently high temperature that the material becomes molten, thereby enabling random (*i.e.*, Brownian-like motion) or driven (*i.e.*, electric field-induced) nanorod re-alignment. The presence of such reorientations provides a lower limit on the temperature of the sample volume surrounding the GNRs (*i.e.*, that the melting temperature of the material has been attained in this region). Furthermore, as the dynamics of GNR rotation are determined by temperature-dependent local viscosity, which can be rigorously calibrated using the reorientation rates observed within uniformly heated samples, the rate of the nanorods reorientation under photothermal heating can be used to infer the average local temperature within the (nanoscale dimensionally-sized) rotational volume.

Overall initial global alignment of an ensemble of GNRs embedded at low loading concentration within thin polymer nanocomposite samples is achieved using external fields during sample fabrication, as briefly described above and in the Experimental methods section. Non-destructive optical detection of the *in situ* orientation of the nanorods occurs through monitoring the transmission of a linearly-polarized, weak probe beam, resonant with one of the LSPRs of the nanorod. As shown in Fig. 1, for the selected LSPR, maximum (minimum) transmission occurs for orthogonal (parallel) alignment of the light field direction of linear-polarization and the axis of the nanorod. Hence, for driven or random motion of the GNRs from the initially aligned arrangement, corresponding changes in the transmission of the probe beam can be observed in time.

A typical experimental calibration measurement sequence follows: PEO : GNR film samples with initially aligned GNRs are conventionally, uniformly heated using a hot plate while nanorod orientation is maintained by applying an electric field at 20 kV cm^{-1} directed parallel to the long axis of the GNRs, referred to as the "holding field". After a stable constant temperature is achieved, a linearly-polarized laser probe beam resonant with the *l*-LSPR of the nanorod transmits through the sample, with its polarization direction orthogonal to the long axis of the nanorod. Maintaining the optical beam at a very low intensity (~2 mW cm^{-2}) insures that photothermal effects induced by the probe beam are negligible. The holding electric field is switched off and a new electric field of the same ampli-

tude but directed parallel to the polarization direction of the probe beam is applied ("driving field"). The transmission of the probe laser beam is monitored as the GNRs undergo forced reorientation to the new preferred alignment direction. Similarly, measurements can be also made without the driving field, in which case the GNRs undergo random rotational motion.

Fig. 3 presents examples of driven nanorod reorientation within a PEO : GNR film at three different homogeneous sample temperatures using a linearly-polarized weak laser beam to probe the *l*-LSPR of the nanorods. For sample temperatures less than the melting temperature of PEO (T_m = 65 °C), no change in probe transmittance is observed (*e.g.*, 62 °C, dark grey triangles). At 70 °C (light grey circles), the nanorods take ~10 minutes to fully reorient. The vertical double arrow and horizontal or vertical rods schematically depict the relative initial (perpendicular) and final (parallel) orientations of the probe polarization direction and the GNRs long axis, respectively. If the sample temperature is raised further (*e.g.*, 84 °C, black squares), the rate of the driven GNR rotation increases, indicated by the curve shifting to lower times. In this manner, rotation curves for uniform sample temperatures from 65–150 °C are measured. Subsequently, similarly observed GNR rotational reorientation occurring under a particular photothermal heating condition (*i.e.*, certain laser intensity) can be matched to one of these curves, enabling the local temperature experienced by the nanorods to be determined.

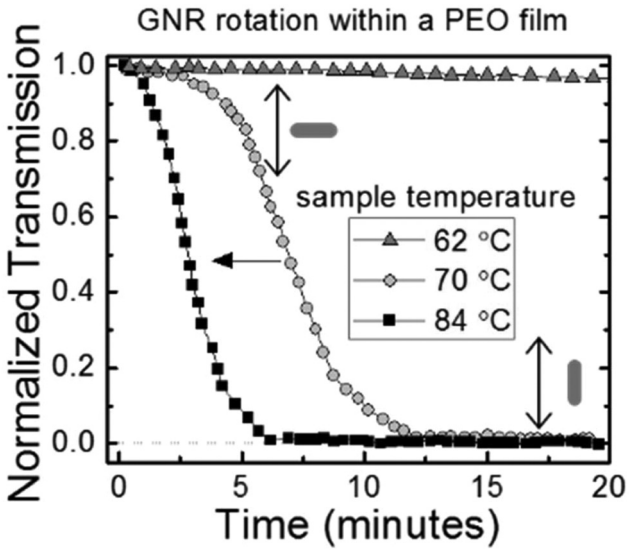

Fig. 3 Observation of GNR rotation under homogeneous heating for three different temperatures. Initially, the polarization direction of the probe field and the GNR orientation direction are orthogonal, thus transmittance is maximized. For average sample temperature below the melting temperature, the transmission signal remains constant (dark grey triangles, 62 °C). As GNRs are driven toward the new alignment direction parallel to the polarization direction, the beam transmission evolves to a minimum (light grey circles, 70 °C). The rate of the GNR reorientation increases with higher sample temperature (black squares, 84 °C), as indicated by the arrow.

Controlling the alignment of GNRs within the nanocomposite sample through application of external fields (light and electric) can be repeated with limited loss of fidelity. Fig. 4a shows a TEM image of an initially, vertically-aligned PEO : GNR film achieved through the second method outlined previously. Subsequently, re-application of the photothermal heating laser and switching the electric field to a (now) horizontally-directed orientation ultimately drives the ensemble of GNRs 90° to a new alignment direction (TEM image, Fig. 4b); thereby, the GNRs within the sample are being controllably pushed from an aligned state to an aligned (with new direction) state. This process can be iterated by switching to an orthogonally-oriented electric field each time complete alignment of the nanorod ensemble is achieved. Hence, in Fig. 4c, the electric field direction is alternatively changed by 90° for 5 consecutive repetitions. Accordingly, though the nanorods do potentially have the ability to also laterally diffuse, there is no evidence of subsequent widespread GNR agglomeration. We note that the slight reduction seen in the probe beam signal extreme values may indicate a small percentage of GNRs are no longer contributing to the measurement. Such a loss might be due to either a low level of aggregation or if the nanorods migrate to the film–substrate glass surface interface and become unable to rotate.

2.3 Presence of a steady-state inhomogeneous temperature distribution and its dependence on nanorod concentration and irradiation intensity

Observations of steady-state local and global temperatures in PEO : GNR nanocomposite films under continuous-wave photothermal heating demonstrate the presence of a sustained temperature gradient, warmest near the nanoparticles and cooler in regions further removed. Fig. 5 shows measurements of the temperature from GNR reorientation (local) and that of the average sample temperature made simultaneously *via* the perylene fluorescence method (global) for the extreme values of nanorod film concentration investigated. In the case of the highest particle concentration employed (2.5 wt% GNR), having an average GNR-to-GNR separation of ~0.27 μm, Fig. 5a reveals that the entire film sample is molten, as the global sample steady-state temperature for all light intensities is above T_m for PEO (indicated by the horizontal dotted line), monotonically rising from an initial value ~65 °C at the lowest laser intensity (0.5 W cm^{-2}) and increasing to ~70 °C at the largest laser intensity employed (4 W cm^{-2}).

In the region close to the nanoparticles, the local steady-state temperature grows commensurately from 75–100 °C with increasing illumination intensity. These observations reveal a temperature difference ΔT of ~17 ± 7 °C between the small regions enveloping the photothermal nanoscale nanorods heaters as compared to the cooler sample volumes further away, with a maximum change of ~30 °C at the highest intensity for this relatively high GNR concentration case. In contrast, for the most dilute GNR loading (average rod-to-rod distance ~1.2 μm between neighboring GNRs), Fig. 5b illustrates that the average sample temperature is only (23–28 °C) slightly

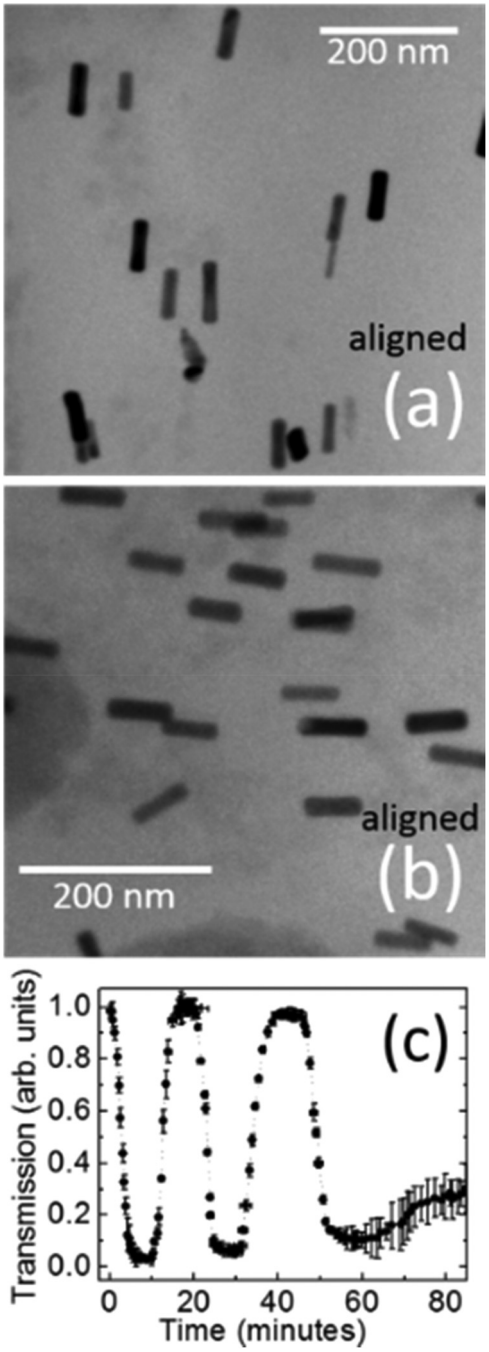

Fig. 4 Recurrent driven GNR alignment. (a) TEM image of a PEO : GNR nanocomposite film sample having initially vertically-aligned nanorods, with an average GNR angular direction of 0 ± 9.2°. (b) TEM image after photothermal heating (4 W cm^{-2} at 514 nm resonant with the *t*-SPR) and a horizontally-oriented electric field of 20 kV cm^{-1}, which causes reorientation of the ensemble GNRs to 90° ± 11.6°. (c) This driven rotational process can be repeated by switching from a parallel- to a (comparatively) perpendicularly-oriented electric field after each complete alignment is achieved. Note: At ~55 minutes, the electric field is turned off, enabling random GNR reorientation.

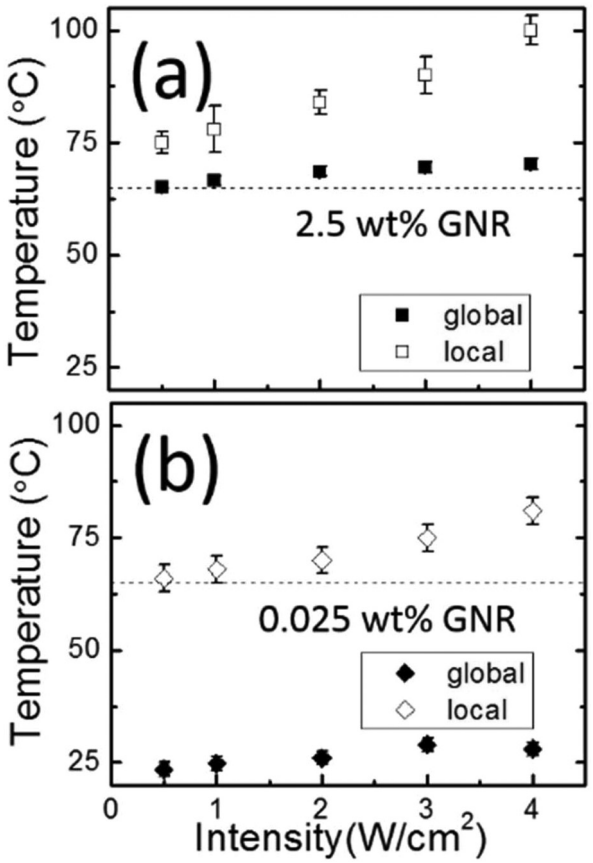

Fig. 5 Observed temperatures within nanocomposite film samples as a function of photothermal heating laser intensity determined near the nanorods by GNR rotation (local) as compared to the overall average measured by fluorescence (global). (a) Under high particle loading (2.5 wt% GNR), and (b) 100× more dilute particular concentration (0.025 wt% GNR), where the horizontal dotted lines correspond to T_m for PEO.

above the ambient value (~21 °C) as the majority of the sample remains relatively cool and solid. However, the temperature in the vicinity of the GNR surpasses T_m, increasing with higher laser intensity from 66–81 °C, creating an average ΔT of ~46 ± 4 °C in this range of irradiation intensities with a maximum change of ~53 °C under the highest illumination condition. These observations make intuitive physical sense in several ways: each particle has a well-defined cross-section for absorption and thus under a particular intensity at a specific wavelength, the energy absorbed per second per particle should be identical. The resultant local and global steady-state temperature will depend on the associated losses and the heat transport within the material. In steady-state, the temperature moving away from each particle to a distance r will fall off as $\sim 1/r^x$, where for a spherical particle in a homogeneous environment (a thick amorphous or liquid sample) $x = 1$ exactly. As particle concentration increases, the global temperature will increase as more total energy is deposited into the system. Thinking of the nanoscale heat profile, if the temperature at each particle is relatively constant and the decrease in temperature with distance (in the simplest approximation, determined by the thermal conductivity) is also fixed, the "tails" of the temperature profile of each heater will overlap

and self-consistently determine the average background temperature far from any particle. As the particle spacing decreases, the distance where neighboring curves overlap also decreases as reflected in an increase in global temperature. Thus, for samples with higher nanoscale heater concentrations, the overall global temperature is increased, the difference between the extreme sample temperature values is reduced, and the temperature within the system is generally spatially more homogeneous. Conversely, for the much larger GNR separations when fewer nanoheaters are present in the sample, ΔT is enhanced as the local, hotter volumes around the nanorods (in this case, molten polymer) are widely-separated within the largely solid, much cooler sample.

Fig. 6 displays additional data over a range of GNR concentrations from 0.025–2.5 wt%: identically-shaped symbols are used for each concentration, filled (open) for the local (global) data. (Data points for 2.5 and 0.025 wt% GNR samples are the same as displayed in Fig. 5.) There are several important points to consider. In each case, the expected behavior of comparatively higher temperatures locally and cooler ones globally, which all increase as the light intensity rises, is observed. For the two lowest concentrations (0.025 and 0.05 wt%, respectively) the global temperature remains below T_m for the entire intensity range. Physically this means that much of the sample is solid, with only small molten regions located around each particle. At 0.25 wt% (corresponding to an average nanorod separation of ~0.57 μm), only at the highest applied laser intensity (4 W cm^{-2}) is the melting point of PEO reached across the entire sample; for the next highest concentration (1 wt%) this level is achieved at 3 W cm^{-2}.

Comparing the sensitivity of the local and global temperatures to nanoparticle concentration, at a given intensity, most of the local temperatures are similar (overlapping within error) whereas the global temperature varies more dramatically from

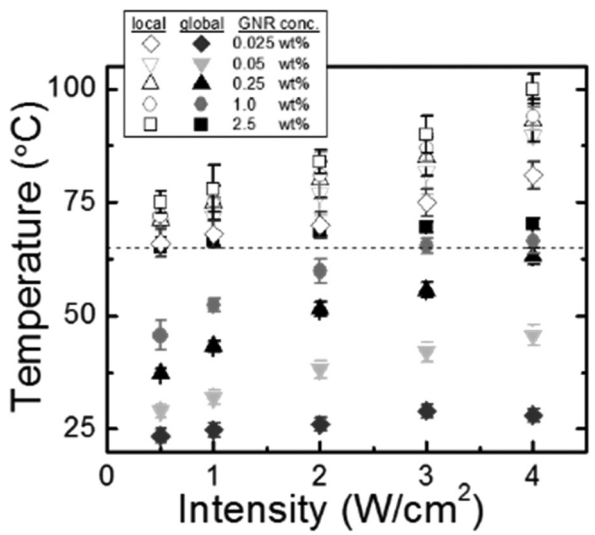

Fig. 6 (a) Observed local *versus* global temperatures for five different nanorod concentrations in a PEO : GNR nanocomposite film. The horizontal dotted line corresponds to the melting temperature of PEO.

essentially room temperature for the lowest concentration to greater than T_m for higher particle loadings. The data indicates that for most concentrations studied, the molten polymer immediately surrounding the particle has a (local) temperature that is relatively independent of concentration. This outcome may be a result of the molten environment, where additional energy loss mechanisms are present compared to the solid sample portions, as well as the consequence of significant changes in the heat capacity and thermal conductivity of PEO near T_m. Such effects can also be observed in the global temperature data. Examining the global temperature for 1 wt% concentration (open circles), when the majority of the material is solid (global temperature below T_m, for intensity <3 W cm^{-2}), increase in temperature with intensity is roughly linear; however upon complete sample melting the curve flattens, with the observed temperature at 4 W cm^{-2} unchanged from that seen at 3 W cm^{-2}. Similarly, for the range of concentrations (all except the lowest) where irradiation of 4 W cm^{-2} intensity results in global temperature near T_m, the data is similarly clustered, with almost no change in global temperature despite a 50× increase in particle concentration. This indicates that significant changes to the thermal properties of the system with temperature make it more difficult to heat in the molten regime, thus decreasing the increase in temperature when energy input increases and causing the data to cluster.

The more dramatic changes in the global temperature (particularly when most of the sample is in solid phase) can be quantitatively understood and analyzed *via* measurement and consideration of thermal loss and changes in thermal losses under different conditions. This case (where most of the sample volume is not molten) can benefit from application of a useful phenomenological model (developed in a previous work[10]) as follows: in steady-state, energy into and out of the system are balanced so that $\frac{Q_{in}}{time} = \frac{Q_{out}}{time}$. Conduction and convection losses depend linearly on temperature difference. Thus, for cases where thermal loss due to radiation is negligible, a rough approximation gives $\frac{Q_{out}}{time} = aT$ where T is an average (global) temperature difference (above the initial room temperature value) and a includes both the coefficients of thermal conductivity and convective heat transfer, as well as the cross-sectional area.[10] Thinking of the system's path to achieving steady-state, $\frac{Q_{in}}{time}$ is constant with time and for any short time increment without a phase transition, $\frac{Q_{in}}{time} - \frac{Q_{out}}{time} = mc\left(\frac{\partial T}{\partial t}\right)$. (We point out that the latent heat of melting needed to transition the sample through this phase transition is relatively small as discussed further in section 2.4; thus most of Q_{in} is available to increase the temperature.) In the simplest analysis, if all heat loss coefficients are temperature independent, the initial loss will be small (due to the small T), the initial $\frac{Q_{in}}{time}$ will lead to an increase in temperature, resulting in a larger $\frac{Q_{out}}{time}$, and this process will continue

until $\frac{Q_{out}}{time} = \frac{Q_{in}}{time}$ at which point steady-state is achieved. Thus, a measure of the losses in the system can be achieved by observing the rate of increase in temperature before steady-state is achieved; in general, the larger the loss coefficients, the shorter the time to steady-state. For the simplest case (constant loss coefficients with temperature), $\frac{\partial T}{\partial t} = B - AT$ where B is defined as $\frac{\left(\frac{Q_{out}}{time}\right)}{mc}$, A is $\frac{a}{mc}$, m is the sample mass and c is the specific heat. The solution to this differential equation is:

$$T = \left(\frac{B}{A}\right)\left(1 - e^{-At}\right) \quad (1)$$

In practice, it is highly unlikely that A will remain constant with temperature and due to the nanoscale nature of photothermal heating, there are in fact many interfaces through which heat transport will occur (resulting in many dissimilar loss terms having varying effective area and temperature differences). However, the pertinent point of the above analysis is that temperature *versus* time before achievement of steady-state reveals useful information about the effective losses present in the system. Quantitative analysis of such temperature *versus* time data enables a deeper understanding and explanation of the resultant global steady-state temperatures (as shown in Fig. 6), as undertaken in the next section.

2.4 Average sample temperature *vs.* time for different GNR concentrations

Fig. 7 shows temperature *versus* time (with t = 0 s the moment the irradiation is first applied) for four different GNR concentrations in PEO : GNR nanocomposite films at three distinct illumination conditions. (Additional curves at other intermediate applied irradiances (0.5 and 3.0 W cm^{-2}) are shown in ESI Fig. S2.†) Generally, for a given illumination intensity, the time to achieve steady-state (which reflects the losses in the system) is faster as GNR concentration is increased. Higher temperatures result in augmented loss mechanisms: for instance, the coefficients associated with natural convention (*e.g.*, air removing heat from the surface of the sample) have a non-linear temperature dependence and polymer melting escalates both conduction and convection processes within the sample. It is crucially important to measure and account for this complex heat loss when analyzing the results of photothermal heating. As an example, at 0.25 wt% loading, a naïve approach might be to expect that increasing the intensity from 0.5 W cm^{-2} to 1 W cm^{-2}, would result in a doubling of T_{ss}, the steady-state temperature above ambient. Fig. 8 includes this data, where the actual observed change is from 17.3 ± 1.5 °C to 23.2 ± 1.5 °C. However, this discrepancy can be resolved by considering the changes in loss coefficients as estimated from the time to achieve steady-state. In particular, accounting for the fact that the effective A (as revealed by the more rapid approach to steady state) has increased by ~1.4× results in an estimate of 24 ± 2 °C, which overlaps the observed value.

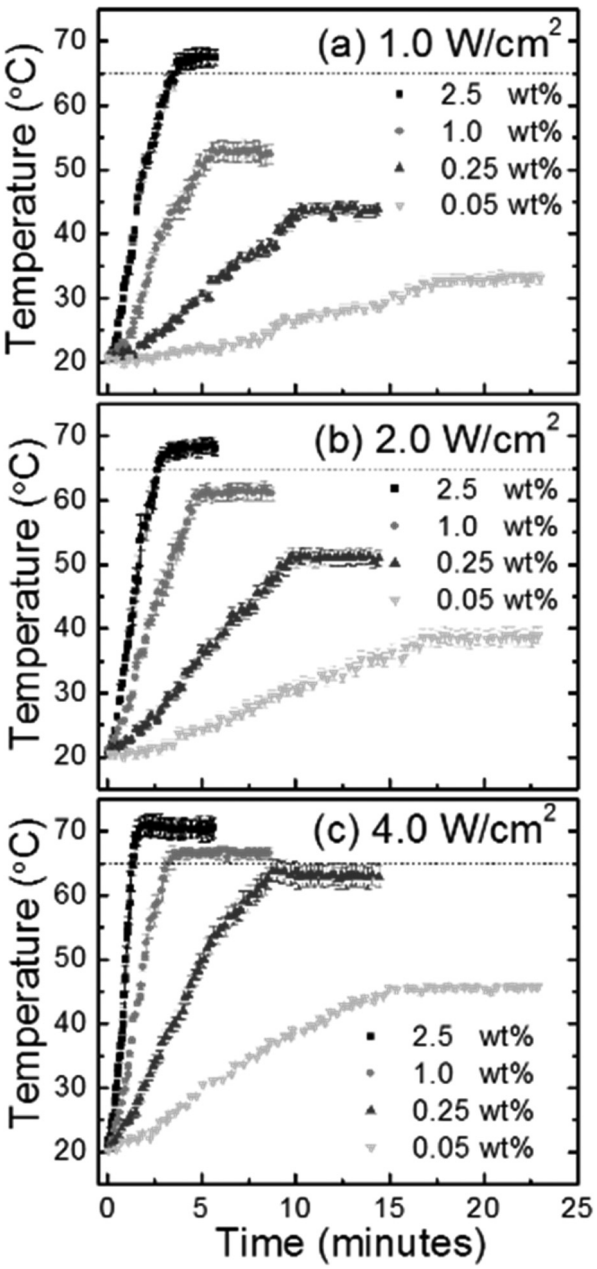

Fig. 7 Global sample temperature measurement *versus* time for different nanoparticle concentrations (0.05, 0.25, 1.0, and 2.5 wt% GNR) as the photothermal laser intensity is doubled from (a) 1.0 W cm^{-2}, to (b) 2.0 W cm^{-2}, and then doubled again to (c) 4.0 W cm^{-2}. See also Fig. S2.†

Fig. 8 displays such an analysis for 0.05, 0.25 and 1.0 wt% GNR concentration film samples where the observed global steady-state temperature rise above ambient is shown as points and the lines are estimates with no adjustable parameters. Each estimate scales the previous lower intensity T value by considering the known change in intensity and adjusting for the measured change in loss. Because it is clear from the data that the temperature *versus* time response (particularly for final global temperatures near T_m) contains several different effective time constants (as expected as discussed at the end of

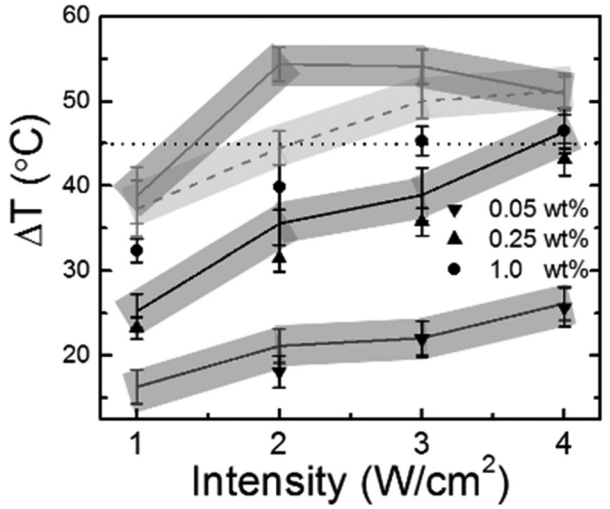

Fig. 8 Global temperature above ambient *versus* applied intensity for 0.05, 0.25 and 1.0 wt% GNR concentration. Fits are straight solid lines, with shaded region displaying confidence bounds. For global sample temperatures below T_m (indicated by the horizontal dotted line), there is good agreement; for conditions where global sample temperatures approach or exceed T_m, such a simple treatment is less effective at modelling the sample's thermal behavior.

section 2.3), a simple approach of determining the time to $0.5 \times T_{ss}$ is taken, where this value is then utilized as an approximate measure of average loss. Thus, in determining increase in thermal losses when changing intensity, the ratio of the $0.5 \times T_{ss}$ time values for the associated cases are employed. Within this approach, one assumption is that the temperature increase is continuous, that is, the time delay associated with latent heat is sufficiently small to be neglected. Given the incoming intensity and the total mass of the film, the associated time delay to melt the entire sample is estimated to be between 0.1 and 0.5 minutes (depending on irradiation intensity and the conversion efficiency), which is insignificant compared to the measured times of a few to tens of minutes as shown in Fig. 7. Returning to Fig. 8, fit of the estimates to the observed data for the lowest GNR concentrations (0.05 wt% and 0.25 wt%) indicates a self-consistency between changes in the speed to reach steady-state and the steady-state values as constrained by the simple model utilized for eqn (1). Thus, the fits of these curves (with no adjustable parameters) indicates that that the full data set is internally consistent and relatively well understood.

As the concentration increases and thus the global temperature approaches T_m (indicated by the horizontal dotted line), the estimates from this simple model are the same order of magnitude as the data but no longer closely fit the observed T_{ss} as a function of intensity (*i.e.*, at 1% loading, the fit and data do not overlap). It is likely that in these cases where A is changing dramatically during the heating process, the simple approach of determining an average value is inadequate. The estimate is improved by focusing on the early time response of the system utilizing the time to $0.1 \times T_{ss}$ to estimate the losses, as shown by the dashed grey line. However in both cases, the estimates are consistently higher than the observed value. This observation is consistent with the previous discussion of data clustering for cases where the local or global sample is molten. Temperature dependent changes in the thermal properties of the system reduce the increase in T_{ss} with increased energy input.

3. Polymeric nanofibers acting as a temperature indicator

Nanofibrous mats consist of layers of randomly oriented fibers of typically ~100–300 nm diameter. Customarily fabricated by some variation of an electrospinning process,[69–74] the resulting samples both have a large surface-to-volume ratio and a high porosity value (~70% open space) which is useful for a wide variety of modern technical applications.[75,76]

Fig. 9a shows a scanning electron microscopy (SEM) image of an as-fabricated mat of PEO : GNR nanofibers having an average fiber diameter of 125 ± 25 nm. During the nanocomposite electrospinning fabrication process, due to the presence of the applied electric field, nanorods self-orient along the fiber axis[12,77] as exemplified in Fig. 9b, a TEM image of several individual nanofibers.[37]

In general, polymeric nanofibers are markedly and irreversibly affected when experiencing temperatures which approach T_m of the matrix material. Due to the very large surface area to volume and suppression of T_m at the surface, once subjected to temperatures at or above approximately T_m −15 °C, the nanofibers begin curling and fusing together and ultimately lose all distinct morphological structure to form a homogeneous featureless film. As shown in Fig. 10a, when heated to 50 °C (T_m −15 °C for PEO), PEO : GNR nanofibers fuse. Similarly, if heated at 70 °C (Fig. 10b), fiber fusion leads to larger structures and loss of distinct fibers. Finally, under conventional heating at 90 °C, complete loss of fibers and film formation is seen (Fig. 10c). Hence, observing the morphology of nanofibers provides an indirect method for discerning

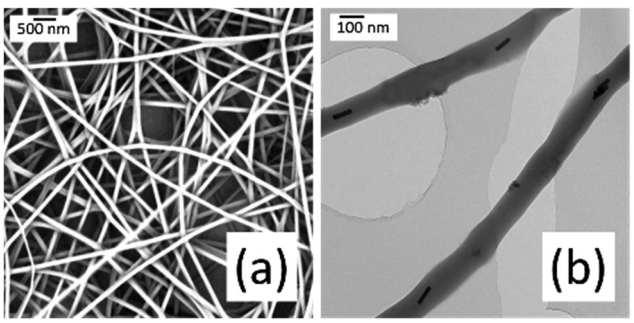

Fig. 9 (a) SEM image of as-fabricated, randomly-arranged, PEO nanofibers containing 0.005 wt% of GNR. (b) Characteristic TEM image of the nanofibers reveal the GNRs align along the fiber axis direction during fabrication.

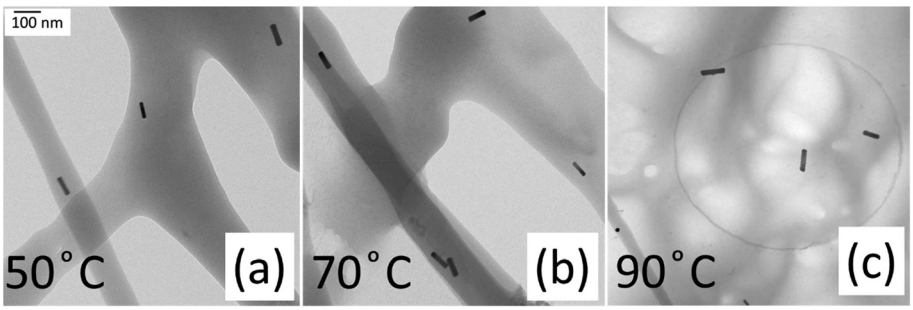

Fig. 10 TEM image of PEO : GNR nanofibers (0.005 wt% nanorods) after 25 minutes of conventional heating at (a) 50 °C, (b) 70 °C, and (c) 90 °C.

information about the thermal history of a sample, and in particular, whether a threshold temperature ($\sim T_m$) was approached or possibly exceeded.

This insight is particularly useful as an indication of surface temperature[37] which can be utilized *ex situ* and as an independent measure of global temperature, synergistic with the molecular thermometry experiments summarized in the previous two sections. Fig. 11a shows an SEM image of nanofibers after exposure to 4 W cm^{-2} green laser light, where from the nanocomposite film results the expectation is that the local temperature (~88 °C in films) around the GNRs will exceed T_m while the global average sample temperature (~34 °C in films) will remain significantly cooler (far below T_m). This example is a particularly illustrative case as the fiber diameter is just slightly larger than the GNR length. Thus the portion of the nanofiber "near" the GNR is the entire fiber segment (a volume approximately 125 nm in diameter and 80–100 nm along the fiber). Indeed, consistent with these previous temperature measurements, except solely in the very immediate spatial regions surrounding the nanoparticles (TEM image Fig. 11b) where occasional fiber breakage occurs, there is no evidence of any larger scale deleterious thermal effects. In contrast with the conventional heating results, there is no observation of any fiber melting, fiber merging or other gross shape changes away from the regions in the immediate vicinity of each GNR. Fig. 11b also illustrates that nanorod reorientation has occurred, which indicates complete melting in the region immediately surrounding the GNR.

These observations are consistent with the results in films in the previous sections, indicating that a large spatial temperature gradient is present at steady-state under photothermal heating with continuous wave light where there are large spatial temperature changes extremely local to the nanoparticle. Overt melting of a short nanoscale segment in conjunction with the remainder of the nanofiber remaining solid is consistent with fiber breakage at the GNR locations.

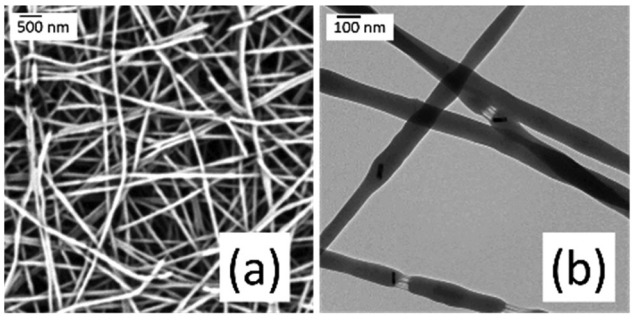

Fig. 11 (a) SEM image of PEO : GNR (0.005 wt% nanorods) after 25 minutes of photothermal treatment with 514 nm light having an intensity of 4 W cm^{-2}. The fibers remain intact with no overt changes in morphology, except for occasional breakages. (b) TEM image of such photothermally-treated fibers reveal the GNRs have undergone random local rotations (are no longer oriented along the fiber axis direction), which indicates that the polymer melted at these locations. Additionally, the fiber breakages and apparent melting occurs exclusively at the GNR sites, consistent with polymer melting in one short region while the rest of the fiber remained solid.

4. Conclusions

Optical nanothermometry under a wide range of nanoparticle loading levels and applied light intensities confirms the presence of a significantly heterogeneous steady-state temperature distribution in the interior of solid polymer films experiencing photothermal heating due to embedded metal nanorods illuminated by continuous wave light resonant with the GNR's localized surface plasmon resonance. Analysis of the global temperature's approach to steady-state and the resultant steady-state temperature measurements demonstrate that the results are self-consistent and compatible with a simple model where the thermal losses in the system can be estimated *via* the measured time to equilibrium. For both local and global temperatures, temperature was relatively insensitive to changes in intensity or nanoparticle concentration (both of which provide linear increase in heat input to the system per time) when the polymer was molten, which is not surprising given the increase in heat loss mechanisms and change in associated coefficients with temperature in this regime. When the polymer is formed into nanofibers the extreme local heating in the vicinity of each GNR lead to melting and fiber breakage at the GNR locations while the remainder of the nanofibers shows no evidence of significant heating.

5. Experimental section

5.1 Materials

Polyethylene oxide (PEO) having molecular weight of 400 kg mol^{-1} was obtained from Scientific Polymer Products. Methanol (UltimAR) from Macron, perylene (99.5%) from Sigma Aldrich, NaOH (98%) from Sigma Aldrich, tetraethoxysilane (99.9%) from Alfa Aesar, and 2-[methooxy(polyethyleneoxy)propyl]9-12-trimethoxysilane (PEG-silane) from Gelest were used as received. The last three chemicals were utilized to create a silica over-coating on the GNR. Perylene, with an initial dispersion in methanol, was incorporated with the polymer to serve as a molecular temperature sensor. All chemicals were used as received. Deionized water (18.2 MΩ) was produced from a laboratory purification system (Evoqua Water Technologies). The glass substrates (Fisherbrand, microscope cover glass 12-540B) were cleaned prior to use with a commercial UV-ozone system (Procleaner 110, Bioforce Nanoscience).

5.2 Gold nanorod synthesis

Produced *via* a seed-mediated growth process,[78] the GNRs had average lengths of 68 ± 7 nm, widths of 17 ± 3 nm, and ARs of 4.0 ± 0.82, as determined by analyzing >100 particles using TEM images of drop-cast samples. Both nanorods which were hexadecyltrimethylammonium bromide (CTAB)-capped, as well as those coated in thin (~4 nm) silica shells[79] were used in this study. In general, the silica shells provide enhanced thermal stability; however under the conditions used in this study, there was no evidence of degradation of uncoated GNRs. We note in addition, PEGylating the surfaces of the silica-coated GNRs by adding PEG-silane resulted in these nanorods having superior solubility in multiple organic solvents.

5.3 Nanocomposite film fabrication

PEO powder (4.0 wt%) was mixed into a GNR-methanol solution, and perylene added (0.09 wt%) to serve as a fluorescent temperature sensors, randomly distributed throughout the bulk sample. The resultant solution was drop-cast onto cleaned glass coverslips to obtain PEO–GNR thin film samples having a thickness of ~8 μm. The observations reported here are independent of the substrate composition or thickness, with the same results obtained (within error) for films deposited on thin glass, thick glass, or sapphire substrates (see ESI Fig. S3†). For the film samples discussed in this report, the concentration of GNRs was varied by 100× over the range from 2.5–0.025 wt% of the final nanocomposite, corresponding to adjusting the average separation between nanorods from 0.26 ± 0.03 to 1.24 ± 0.03 μm. Two methods were used to create nanocomposite samples having GNRs with large-scale alignment. For the first, external parallel electrodes applied a homogeneous DC electric field (~20 kV cm^{-1}) while drop-cast samples were dried under ambient conditions (~1 hour) in order to orient the GNRs' long axes along the applied field direction. In the second approach, a fully dried film with random GNR orientation was exposed to high intensity, circularly-polarized light (4 W cm^{-2} @ 514 nm) resonant with the *t*-LSPR for ~10 minutes under ambient conditions, while the DC electric field was simultaneously applied. Subsequently, the light is blocked and the electric field left on for ~1 hour as the sample cools.

5.4 Nanocomposite fiber fabrication

A PEO : GNR : perylene : water solution was prepared and mixed using a magnetic stirrer; the PEO (perylene) was at 4 (0.09) wt% relative to the total water content; GNRs in water could be added at varying dilutions, which results in 2.5–0.005 wt% in the final nanocomposite. After stirring overnight, the solution was single-needle electrospun[80] using a syringe-pump (New Era Pump Systems, Model NE 500) at a feed rate of 6 μL per minute with a positive-polarity needle-to-collector applied voltage of 15 kV (Glassman High Voltage, Model no. FC60R2) and a needle-to-collector working distance of 20 cm. The collector was electrically grounded. The nanofibers are gathered in layers having random fiber orientation onto glass coverslips affixed to aluminum foil on the collector; or directly onto aluminum stubs or copper grids for electron microscopy analysis. Well-formed cylindrical nanofibers were fabricated having ~125 ± 25 nm in diameter, analyzing multiple SEM images using Image J software.

5.5 Illumination sources

The photothermal excitation light was produced by a commercial water-cooled Ar^+ continuous-wave laser (Coherent Innova Sabre R ML 14). The multi-line output was dispersed with a prism, enabling only the narrow single, spectral line at 514 nm to be used. The linearly-polarized excitation beam is made circularly-polarized using a quarter-wave plate, then expanded and collimated to ~5 mm diameter ($1/e^2$ value) before illuminating the sample, acting as the cw photothermal heating beam. The average light intensity could be varied using the laser power supply, enabling controlled intensity over a range of 0.5–4 W cm^{-2}. Internal laser feedback control enabled power stabilization (≲3% amplitude variation) during experimental runs. Commercial diode lasers were used to generate the red 808 nm (Kales CNCs laser modules) and violet 405 nm (maXYZmodules) beams used in temperature measurements. GNR rotation utilized the 808 nm laser beam collimated to ~2 mm diameter (~$1/e^2$ value) and made weak in power (~50 μW). Average (global) sample temperature measurements used a 405 nm continuous-wave diode laser, expanded and collimated to ~3 mm diameter (~$1/e^2$ value) to excite the homogeneously-distributed perylene molecules. All three beams are spatially well-overlapped on the sample.

5.6 Sample characterization

SEM images (FEI Phenom-World BV) were used to characterize the nanofibers while TEM measurements were performed (JEOL 2000FX) in order to analyze the dimensions of the GNRs and their orientations within the thin film and nanofiber samples.

5.7 Temperature measurements

Method #1: Full spectrum perylene fluorescence was detected after 405 nm excitation by using a double-grating scanning monochromator (SPEX 1680B), with the output beam detected by a side-on photomultiplier tube (PMT) detector (Hamamatsu 931B) coupled to a homemade amplifier. The amplified signal enabled photon counting (Stanford Research System SR 400) with a subtracted background correction by counting equal times with the excitation source blocked. Temperature values are inferred by comparing amplitude ratio values at trough (~465 nm) and peak (~480 nm) features under homogeneous, uniform heating conditions using a commercial hot plate (VWR 7 × 7 CER), to those generated during photothermal heating of the GNRs. Scattered light was selected against by using dielectric interference filters. The overall system resolution was <1 nm. Method #2: To directly observe GNR rotation, the 808 nm laser beam was made extremely weak and optically amplitude-modulated at a 2 kHz rate with a flywheel chopper (Stanford Research Systems SR540), then detected after transmission through the sample by a photodiode (Thorlabs DET36A) whose signal was fed to a lockin amplifier (EG&G Princeton Applied Research Model 5209) referenced to the chopper frequency. The linear-polarization direction of the probe laser was oriented perpendicularly to the initial GNR ensemble alignment. A DC electric field along the initial GNR alignment direction (holding field) maintained the particles' orientation for ~15 minutes under cw photothermal excitation until a stable, steady-state sample temperature (as determined by method #1) is achieved. Then, simultaneously, the field was turned off and a new electric field oriented orthogonally to the first was applied (driving field), and the probe transmittance subsequently monitored. The temperature was calibrated by comparison of the rate of GNR rotation to curves generated by samples which were heated conventionally using the hot plate. Note: While the absolute rate of rotation reorientation (either driven by an external electric field or freely, randomly diffusing) was GNR coating-dependent, this effect is accounted for by the calibration procedure and types of rods showed the same resultant measured temperature within error.

Acknowledgements

This research was supported by the National Science Foundation (grants CMMI-0829379, CMMI-106910, DMR-1056653, and the Research Triangle MRSEC DMR-1121107) and Sigma Xi (GIAR). This work was performed in part at the Analytical Instrumentation Facility (AIF) at North Carolina State University, which is supported by the State of North Carolina and the National Science Foundation (grant ECCS-1542015). The AIF is a member of the North Carolina Research Triangle Nanotechnology Network (RTNN), a site in the National Nanotechnology Coordinated Infrastructure (NNCI). Additionally, the authors thank the NC State Physics Education and Research Laboratory (EaRL), Prof. Keith Weninger (NCSU), and Prof. Albert Young (NCSU) for use of equipment, and Dr Jeffrey Meth (E. I. DuPont de Nemours & Co., Inc) for previous discussions regarding heating mechanisms.

References

1 C. F. Bohren and D. R. Huffman, *Absorption and scattering of light by small particles*, Wiley, Weinheim, Germany, 2004.
2 T. Ming, H. J. Chen, R. B. Jiang, Q. Li and J. F. Wang, *J. Phys. Chem. Lett.*, 2012, **3**, 191–202.
3 S. Park, M. Pelton, M. Liu, P. Guyot-Sionnest and N. F. Scherer, *J. Phys. Chem. C*, 2007, **111**, 116–123.
4 C. J. Murphy, T. K. San, A. M. Gole, C. J. Orendorff, J. X. Gao, L. Gou, S. E. Hunyadi and T. Li, *J. Phys. Chem. B*, 2005, **109**, 13857–13870.
5 M. J. A. Hore and R. J. Composto, *Macromolecules*, 2014, **47**, 875–887.
6 G. Baffou and R. Quidant, *Chem. Soc. Rev.*, 2014, **43**, 3898–3907.
7 L. Y. Cao, D. N. Barsic, A. R. Guichard and M. L. Brongersma, *Nano Lett.*, 2007, **7**, 3523–3527.
8 T. K. Sau, A. L. Rogach, F. Jackel, T. A. Klar and J. Feldmann, *Adv. Mater.*, 2010, **22**, 1805–1825.
9 J. Dong, G. E. Firestone, J. R. Bochinski, L. I. Clarke and R. E. Gorga, *Nanotechnology*, 2017, **28**, 065601.
10 S. Maity, J. R. Bochinski and L. I. Clarke, *Adv. Funct. Mater.*, 2012, **22**, 5259–5270.
11 S. Maity, L. N. Downen, J. R. Bochinski and L. I. Clarke, *Polymer*, 2011, **52**, 1674–1685.
12 S. Maity, K. A. Kozek, W.-C. Wu, J. B. Tracy, J. R. Bochinski and L. I. Clarke, *Part. Part. Syst. Charact.*, 2013, **30**, 193–202.
13 V. Viswanath, S. Maity, J. R. Bochinski, L. I. Clarke and R. E. Gorga, *Macromolecules*, 2013, **46**, 8596–8607.
14 V. Viswanath, S. Maity, J. R. Bochinski, L. I. Clarke and R. E. Gorga, *Macromolecules*, 2016, **49**, 9484–9492.
15 O. Neumann, C. Feronti, A. D. Neumann, A. Dong, K. Schell, B. Lu, E. Kim, M. Quinn, S. Thompson, N. Grady, P. Nordlander, M. Oden and N. J. Halas, *Proc. Natl. Acad. Sci. U. S. A.*, 2013, **110**, 11677–11681.
16 Y. Xiong, R. Long, D. Liu, X. Zhong, C. Wang, Z.-Y. Li and Y. Xie, *Nanoscale*, 2012, **4**, 4416–4420.
17 M. T. Quint, S. Delgado, J. H. Paredes, Z. S. Nuno, L. S. Hirst and S. Ghosh, *Opt. Express*, 2015, **23**, 6888–6895.
18 Y. Zhou, A. W. Hauser, N. P. Bende, M. G. Kuzyk and R. C. Hayward, *Adv. Funct. Mater.*, 2016, **26**, 5447–5452.
19 D. B. Abbott, S. Maity, M. T. Burkey, R. E. Gorga, J. R. Bochinski and L. I. Clarke, *Macromol. Chem. Phys.*, 2014, **215**, 2345–2356.
20 D. Jaque, L. M. Maestro, B. del Rosal, P. Haro-Gonzalez, A. Benayas, J. L. Plaza, E. M. Rodriguez and J. G. Sole, *Nanoscale*, 2014, **6**, 9494–9530.
21 A. M. Alkilany, L. B. Thompson, S. P. Boulos, P. N. Sisco and C. J. Murphy, *Adv. Drug Delivery Rev.*, 2012, **64**, 190–199.
22 N. J. Halas, *Nano Lett.*, 2010, **10**, 3816–3822.

23 D. Jaque and F. Vetrone, *Nanoscale*, 2012, **4**, 4301–4326.
24 *Thermometry at the Nanoscale: Techniques and Selected Applications*, ed. L. D. Carlos and F. Palacio, The Royal Society of Chemistry, Cambridge, 2016, vol. 38.
25 G. Baffou, M. P. Kreuzer, F. Kulzer and R. Quidant, *Opt. Express*, 2009, **17**, 3291–3298.
26 S. Balabhadra, M. L. Debasu, C. D. S. Brites, L. A. O. Nunes, O. L. Malta, J. Rocha, M. Bettinelli and L. D. Carlos, *Nanoscale*, 2015, **7**, 17261–17267.
27 M. L. Debasu, D. Ananias, I. Pastoriza-Santos, L. M. Liz-Marzan, J. Rocha and L. D. Carlos, *Adv. Mater.*, 2013, **25**, 4868–4874.
28 F. Vetrone, R. Naccache, A. Zamarron, A. J. de la Fuente, F. Sanz-Rodriguez, L. M. Maestro, E. M. Rodriguez, D. Jaque, J. G. Sole and J. A. Capobianco, *ACS Nano*, 2010, **4**, 3254–3258.
29 D. Wawrzynczyk, A. Bednarkiewicz, M. Nyk, W. Strek and M. Samoc, *Nanoscale*, 2012, **4**, 6959–6961.
30 B. Van de Broek, D. Grandjean, J. Trekker, J. Ye, K. Verstreken, G. Maes, G. Borghs, S. Nikitenko, L. Lagae, C. Bartic, K. Temst and M. J. Van Bael, *Small*, 2011, **7**, 2498–2506.
31 P. R. Ohodnicki, M. P. Buric, T. D. Brown, C. Matranga, C. J. Wang, J. Baltrus and M. Andio, *Nanoscale*, 2013, **5**, 9030–9039.
32 J. B. Herzog, M. W. Knight and D. Natelson, *Nano Lett.*, 2014, **14**, 499–503.
33 P. Neumann, I. Jakobi, F. Dolde, C. Burk, R. Reuter, G. Waldherr, J. Honert, T. Wolf, A. Brunner, J. H. Shim, D. Suter, H. Sumiya, J. Isoya and J. Wrachtrup, *Nano Lett.*, 2013, **13**, 2738–2742.
34 H. T. Sun, M. P. Yu, X. Sun, G. K. Wang and J. Lian, *J. Phys. Chem. C*, 2013, **117**, 3366–3373.
35 Y. Liu, E. N. Mills and R. J. Composto, *J. Mater. Chem.*, 2009, **19**, 2704–2709.
36 W. J. Kennedy, K. A. Slinker, B. L. Volk, H. Koerner, T. J. Godar, G. J. Ehlert and J. W. Baur, *ACS Appl. Mater. Interfaces*, 2015, **7**, 27624–27631.
37 S. Maity, W.-C. Wu, C. Xu, J. B. Tracy, K. Gundogdu, J. R. Bochinski and L. I. Clarke, *Nanoscale*, 2014, **6**, 15236–15247.
38 P. Keblinski, D. G. Cahill, A. Bodapati, C. R. Sullivan and T. A. Taton, *J. Appl. Phys.*, 2006, **100**, 054305.
39 A. Hatef, S. Fortin-Deschenes, E. Boulais, F. Lesage and M. Meunier, *Int. J. Heat Mass Transfer*, 2015, **89**, 866–871.
40 H. H. Richardson, Z. N. Hickman, A. O. Govorov, A. C. Thomas, W. Zhang and M. E. Kordesch, *Nano Lett.*, 2006, **6**, 783–788.
41 D. K. Roper, W. Ahn and M. Hoepfner, *J. Phys. Chem. C*, 2007, **111**, 3636–3641.
42 D. Lapotko, *Opt. Express*, 2009, **17**, 2538–2556.
43 O. Neumann, A. S. Urban, J. Day, S. Lal, P. Nordlander and N. J. Halas, *ACS Nano*, 2013, **7**, 42–49.
44 H. H. Richardson, M. T. Carlson, P. J. Tandler, P. Hernandez and A. O. Govorov, *Nano Lett.*, 2009, **9**, 1139–1146.
45 S. Hwang, J. Nam, S. Jung, J. Song, H. Doh and S. Kim, *Nanomedicine*, 2014, **9**, 2003–2022.
46 L. Bonderer, D. I. Uhlenhaut, P. Smith and W. Caseri, *Materials*, 2014, **7**, 1899–1911.
47 D. A. Boyne, A. M. Savage, M. H. Griep, F. L. Beyer and J. A. Orlicki, *Polymer*, 2017, **110**, 250–259.
48 J. Chen, Y. H. Jin, N. Fahruddin and J. X. Zhao, *Langmuir*, 2013, **29**, 1584–1591.
49 R. C. Ferrier, H. S. Lee, M. J. A. Hore, M. Caporizzo, D. M. Eckmann and R. J. Composto, *Langmuir*, 2014, **30**, 1906–1914.
50 M. J. A. Hore and R. J. Composto, *ACS Nano*, 2010, **4**, 6941–6949.
51 G. Q. Jiang, M. J. A. Hore, S. Gam and R. J. Composto, *ACS Nano*, 2012, **6**, 1578–1588.
52 A. Regiel-Futyra, M. Kus-Liskiewicz, V. Sebastian, S. Irusta, M. Arruebo, G. Stochel and A. Kyziol, *ACS Appl. Mater. Interfaces*, 2015, **7**, 1087–1099.
53 Z. X. Qian, K. N. Guye, D. J. Masiello and D. S. Ginger, *J. Phys. Chem. B*, 2017, **121**, 1092–1099.
54 C. W. Park, A. B. South, X. B. Hu, C. Verdes, J. D. Kim and L. A. Lyon, *Colloid Polym. Sci.*, 2011, **289**, 583–590.
55 D. Lee, S. Jeong, J. H. Park, S. Y. Park and D. J. Jang, *J. Mater. Sci.*, 2016, **51**, 9669–9678.
56 S. Sharma, P. J. Bora, P. Gogoi, R. Boruah, K. J. Mohan and S. K. Dolui, *J. Mater. Sci.: Mater. Electron.*, 2015, **26**, 5465–5474.
57 Z. W. Xiao, Q. Wu, S. D. Luo, C. Zhang, J. Baur, R. Justice and T. Liu, *Part. Part. Syst. Charact.*, 2013, **30**, 338–345.
58 H. J. Zhang, J. M. Zhang, X. Tong, D. L. Ma and Y. Zhao, *Macromol. Rapid Commun.*, 2013, **34**, 1575–1579.
59 A. W. Hauser, D. Q. Liu, K. C. Bryson, R. C. Hayward and D. J. Broer, *Macromolecules*, 2016, **49**, 1575–1581.
60 X. Y. Liu, X. G. Wang, T. Liu and P. Keller, *Macromolecules*, 2016, **49**, 8322–8331.
61 S. Y. Liu, J. F. Li and Z. Y. Li, *Adv. Opt. Mater.*, 2013, **1**, 227–231.
62 S. Stoenescu, V. V. Truong and M. Packirisamy, *Plasmonics*, 2014, **9**, 299–307.
63 B. M. I. van der Zande, G. J. M. Koper and H. N. W. Lekkerkerker, *J. Phys. Chem. B*, 1999, **103**, 5754–5760.
64 P. Zijlstra, M. van Stee, N. Verhart, Z. Y. Gu and M. Orrit, *Phys. Chem. Chem. Phys.*, 2012, **14**, 4584–4588.
65 S. W. Allison and G. T. Gillies, *Rev. Sci. Instrum.*, 1997, **68**, 2615–2650.
66 J. F. Lou, T. M. Finegan, P. Mohsen, T. A. Hatton and P. E. Laibinis, *Rev. Anal. Chem.*, 1999, **18**, 235–284.
67 K. F. Schrum, A. M. Williams, S. A. Haerther and D. Benamotz, *Anal. Chem.*, 1994, **66**, 2788–2790.
68 S. Li, K. Zhang, J. M. Yang, L. W. Lin and H. Yang, *Nano Lett.*, 2007, **7**, 3102–3105.
69 M. P. Roman, N. M. Thoppey, R. E. Gorga, J. R. Bochinski and L. I. Clarke, *Macromolecules*, 2013, **46**, 7352–7362.
70 N. M. Thoppey, J. R. Bochinski, L. I. Clarke and R. E. Gorga, *Polymer*, 2010, **51**, 4928–4936.

71 N. M. Thoppey, J. R. Bochinski, L. I. Clarke and R. E. Gorga, *Nanotechnology*, 2011, **22**, 345301.
72 N. M. Thoppey, R. E. Gorga, J. R. Bochinski and L. I. Clarke, *Macromolecules*, 2012, **45**, 6527–6537.
73 N. M. Thoppey, R. E. Gorga, L. I. Clarke and J. R. Bochinski, *Polymer*, 2014, **55**, 6390–6398.
74 Q. Q. Wang, C. K. Curtis, N. M. Thoppey, J. R. Bochinski, R. E. Gorga and L. I. Clarke, *Mater. Res. Express*, 2014, **1**, 045302.
75 S. Ramakrishna, K. Fujihara, W. E. Teo, T. Yong, Z. W. Ma and R. Ramaseshan, *Mater. Today*, 2006, **9**, 40–50.
76 S. Agarwal, J. H. Wendorff and A. Greiner, *Polymer*, 2008, **49**, 5603–5621.
77 K. E. Roskov, K. A. Kozek, W.-C. Wu, R. K. Chhetri, A. L. Oldenburg, R. J. Spontak and J. B. Tracy, *Langmuir*, 2011, **27**, 13965–13969.
78 K. A. Kozek, K. M. Kozek, W.-C. Wu, S. R. Mishra and J. B. Tracy, *Chem. Mater.*, 2013, **25**, 4537–4544.
79 W.-C. Wu and J. B. Tracy, *Chem. Mater.*, 2015, **27**, 2888–2894.
80 D. H. Reneker, A. L. Yarin, E. Zussman and H. Xu, in *Advances in Applied Mechanics*, ed. H. Aref and E. VanDerGiessen, Elsevier Academic Press Inc, San Diego, 2007, vol. 41, pp. 43–195.

Electronic Supplementary Material (ESI) for Nanoscale.

Supporting Information

Nanoscale Steady-state Temperature Gradients within Polymer Nanocomposites Undergoing Continuous-Wave Photothermal Heating from Gold Nanorods

*Somsubhra Maity, Wei-Chen Wu, Joseph B. Tracy, Laura I. Clarke, and Jason R. Bochinski**

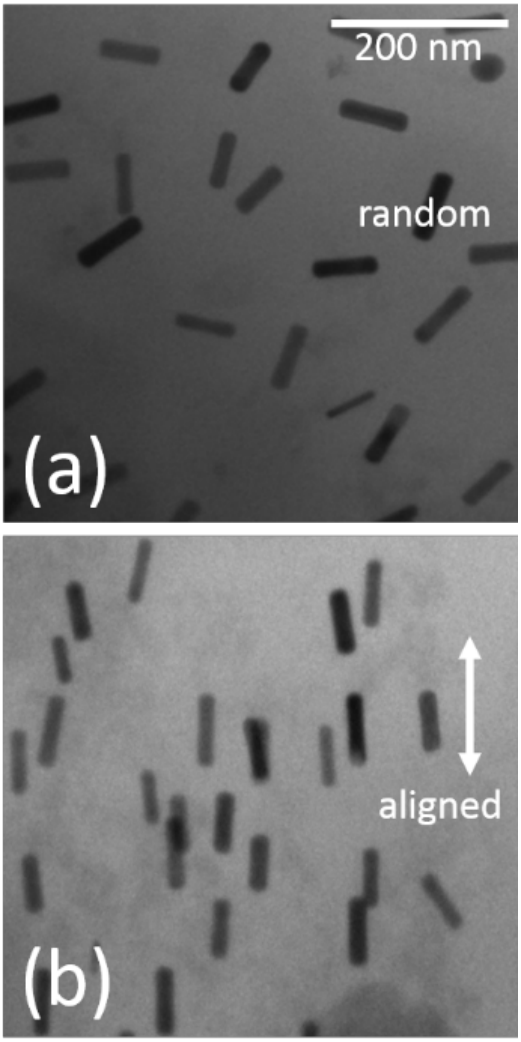

Figure S1. Photothermal- and field-assisted GNR alignment. (a) TEM image of as-fabricated PEO:GNR film having random nanorod orientations. Scale bar applies to both images. (b) TEM image same type of nanocomposite film after photothermal heating (4 W/cm^2 at 514 nm) simultaneously with an applied electric field of 20 kV/cm, resulting in global alignment (0 ± 8.1°) of the GNRs.

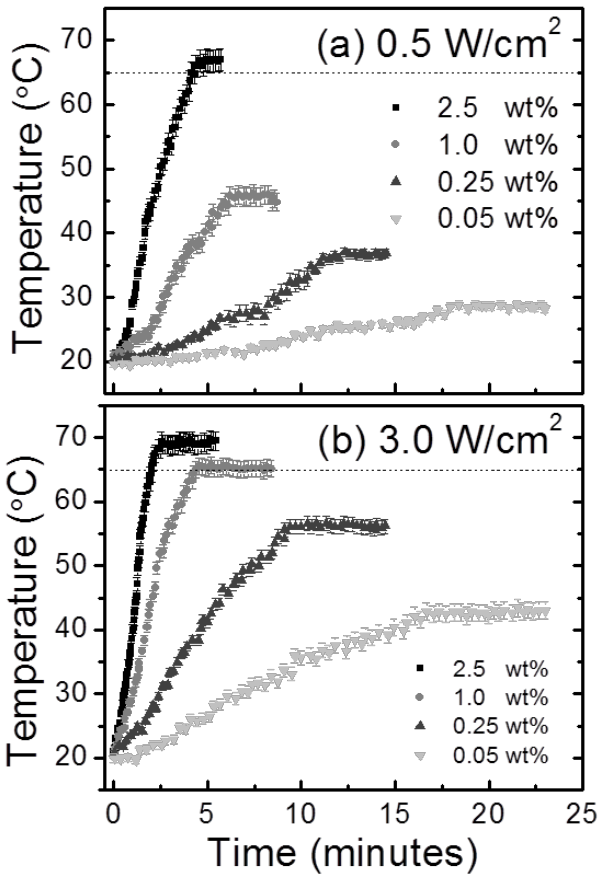

Figure S2. Average global sample temperature versus time for different GNR concentrations observed under different 514 nm illumination intensities, such as (a) 0.5 W/cm^2, and (b) 3.0 W/cm^2. Horizontal dotted lines in both graphs indicate T_m for PEO.

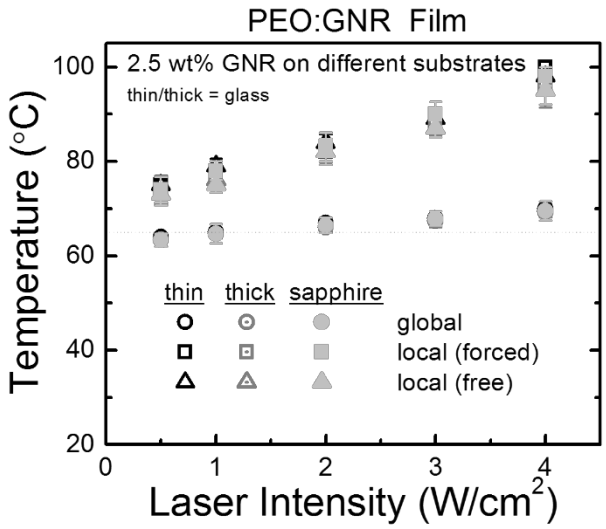

Figure S3. Temperature measurements are independent of substrate material composition or thickness. For thin PEO:GNR films containing 2.5 wt% nanorods, the average sample measurements (circle symbols) from observing perylene fluorescence as well as those from GNR reorientation rotational dynamics in both driven (forced, square symbols) or random (free, triangle symbols) modes, provide reproducible temperature values which overlap within error, reflecting the differences in the local versus the global temperatures. Thin and thick refer to glass substrates of varying thicknesses.